

## **Modeling early radiation DNA damage occurring during [ $^{177}\text{Lu}$ ]Lu-DOTA-[Tyr<sup>3</sup>]octreotate radionuclide therapy**

Giulia Tamborino<sup>1,2†</sup>, Yann Perrot<sup>3</sup>, Marijke De Saint-Hubert<sup>1</sup>, Lara Struelens<sup>1</sup>, Julie Nonnekens<sup>2,4</sup>, Marion De Jong<sup>2</sup>, Mark W. Konijnenberg<sup>2</sup>, Carmen Villagrasa<sup>4</sup>

<sup>1</sup>Research in Dosimetric Applications, Belgian Nuclear Research Centre (SCK CEN), Mol, Belgium.

<sup>2</sup>Department of Radiology & Nuclear Medicine, Erasmus MC Cancer Institute, Erasmus University Medical Center, Rotterdam, The Netherlands

<sup>3</sup>IRSN, Institut de Radioprotection et de Sûreté Nucléaire, Fontenay aux Roses, France

<sup>4</sup>Department of Molecular Genetics, Oncode Institute, Erasmus MC Cancer Institute, Erasmus University Medical Center, Rotterdam, The Netherlands

First author and corresponding author<sup>†</sup>: **Giulia Tamborino**, Research in Dosimetric Application, Belgian Nuclear Research Centre (SCK CEN), Boeretang 200, 2400 Mol, Belgium, Tel: +32 471 99 66 09, Email: [gtambori@sckcen.be](mailto:gtambori@sckcen.be), PhD student.

**Words:** 7000

**Financial support:** None

**Running title:** Modelling DSBs for PRRT

**Immediate Open Access:** Creative Commons Attribution 4.0 International License (CC BY) allows users to share and adapt with attribution, excluding materials credited to previous publications.

License: <https://creativecommons.org/licenses/by/4.0/>.

Details: <https://jnm.snmjournals.org/page/permissions>.



## ABSTRACT

**Rationale:** The aim of this study is to build a simulation framework to evaluate the number of DNA double strand breaks (DSBs) induced by *in vitro* targeted radionuclide therapy (TRT). This work represents the first step towards exploring underlying biological mechanisms and influence of physical/chemical parameters to enable a better response prediction in patients. We used this tool to characterize early DSB induction by  $^{177}\text{Lu}$ -DOTA-[Tyr3]octreotate ( $^{177}\text{Lu}$ -DOTATATE), a commonly used TRT for neuroendocrine tumors.

**Methods:** A multiscale approach is implemented to simulate the number of DSBs produced over 4 h by the cumulated decays of  $^{177}\text{Lu}$  distributed according the somatostatin receptor-binding. The approach involves 2 sequential simulations performed with Geant4/Geant4-DNA. The radioactive source is sampled according to uptake experiments on the distribution of activities within the medium and the planar cellular cluster, assuming instant and permanent internalization. A phase space (PHSP) is scored around the nucleus of the central cell.

Then, the PHSP is used to generate particles entering the nucleus containing a multi-scale description of the DNA in order to score the number of DSBs per particle source. The final DSB computations are compared to experimental data, measured by immunofluorescent detection of 53BP1 foci.

**Results:** The probability of electrons reaching the nucleus was significantly influenced by the shape of the cell compartment, causing large variance in the induction pattern of DSBs.

A significant difference was found in the DSBs induced by activity distributions in cell and medium, which is explained by the specific energy ( $z$ ) distributions. The average number of simulated DSBs is 14 DSBs/cell (range: 7-24 DSBs/cell) compared to 13 DSBs/cell (2-30)

experimentally determined. We found a linear correlation between the mean absorbed dose to the nucleus and the number of DSBs/cell: 0.014 DSBs/cell mGy<sup>-1</sup> for internalization in the Golgi apparatus and 0.017 DSBs/cell mGy<sup>-1</sup> for internalization in the cytoplasm.

**Conclusion:** This simulation tool can lead to more reliable absorbed dose to DNA correlation and help in prediction of biological response.

**Key Words:** DNA double strand break simulation, targeted radionuclide therapy, <sup>177</sup>Lu-DOTATATE, Dose-effect relationship, Geant4-DNA

## INTRODUCTION

The most common way of exposing cancer patients to radiation is through external beam radiotherapy (EBRT). The success and effectiveness of EBRT can, at least partially, be attributed to the knowledge of its radiobiological principles and their integration into dose-response modelling (1).

An alternative form of anti-cancer therapy is targeted radionuclide therapy (TRT). TRT is based on the injection of a radiolabeled molecule which has the advantage of targeting specific cancer cells, enabling the delivery of a cytotoxic absorbed dose to eradicate both a primary tumor site and metastases (2).

In striking contrast to EBRT, TRT is marked by the scarcity of radiobiological investigations and dose-response modelling. The physical characteristics of TRT, i.e. heterogeneous radiation caused by variable uptake at cellular and subcellular level, protracted exposure causing overlapped biological mechanisms such as DNA damage formation and repair and low dose-rate, differ significantly from EBRT, hence TRT-specific radiobiological knowledge and biophysical modelling need to be developed (3).

The initial step into understanding the cell's radiobiological response is represented by the calculation of the energy deposition at subcellular scale and in particular, in the cell nucleus where radioinduced DNA damage can be considered as a key biological output for predicting cellular fate (4). Ultimately, a mechanistically-informed model, including the cell's response dependence on phenotype, cell cycle, micro-environment, type of radiation and delivery method, would allow to understand the underlying biological mechanisms and hence make predictions on the radiosensitivity of individual tissues under a particular irradiation condition (5).

DNA is recognized as a key target and currently, simulations of *in vitro* DNA damage in the context of TRT have been primarily focused on low energetic electrons, namely Auger electrons (e.g.  $^{125}\text{I}$ -Iodo-2'-deoxyuridine,  $^{111}\text{In}$ -DTPA-D-Phe1-octreotide and  $^{64}\text{CuCl}_2$ ), because of their significant decrease in energy density as a function of distance in nanometers (6).

Various models of DNA targets from DNA linear fragments represented by structured cylinders (7) to either simplified (8) or complex atomic representations (9,10) have been used for this purpose using various Monte Carlo codes.

On the other hand, the combination of pre-calculated cluster DNA damage yields by Monte Carlo Damage Simulation code (MCDS) (11) and local dose distributions within a local effect model (LEM) was used as alternative “fast” approach (12).

For Auger emitters internalized in the nucleus, the choice of DNA model and radionuclide placement with respect to the DNA structure, are the main parameters influencing the resulting DSBs computation (10) because of their nm-range. As a consequence, cell morphology and cell population are not modelled in this scenario. On the contrary, longer range radionuclides, such as  $^{177}\text{Lu}$ , require a detailed cell morphology and population modeling to account for both self- and cross-irradiation in a planar cell colony (13). Furthermore, once the irradiation field has been characterized, an “event by event” description of the radiation track structure at the nanometer level within the nucleus, combined with a simulation including description of the target at the relevant scale (e.g. atom, molecule) need to be adopted in order to yield conclusion with regard to the biophysical mechanisms involved. In this respect, faster Monte Carlo approaches for DSBs simulation, intrinsically relying on uniform external irradiation parameters, would not provide a

deeper understanding of the mechanisms involved and as such, would not help to contribute to the final goal of developing methods to select the best approach for individualized treatment optimization. In a similar way, nanodosimetric simulations calculating the ionization cluster size distributions in water cylinders corresponding to DNA segments (14) rely on adjustable parameters – inferred from EBRT exposure - to account for the missing geometrical DNA details and, hence, would not completely serve this purpose.

A successful example of TRT, leading to markedly prolonged survival and better quality of life in comparison to non-radioactive targeted therapy (15,16) is  $^{177}\text{Lu}$ -DOTA-[Tyr<sup>3</sup>]octreotate ( $^{177}\text{Lu}$ -DOTATATE).  $^{177}\text{Lu}$ -DOTATATE treatment targets tumor cells overexpressing the somatostatin receptor type-2 (SSTR<sub>2</sub>) and is authorized in Europe and USA for therapy of metastasized neuroendocrine tumors (NET) as Lutathera® (17).

This work, propose a simulation framework evaluating the number of DNA DSBs occurring during in vitro  $^{177}\text{Lu}$ -DOTATATE experiments with planar colonies, thereby accounting for detailed cellular morphologies and source localizations. We analyzed the impact of different modelling assumptions and compared them with experimental data. This study represents a first step towards a better understanding of the underlying biological mechanisms of  $^{177}\text{Lu}$ -DOTATATE exposure by providing a detailed description of early DSB distribution.

## **MATERIALS AND METHODS**

A two-step simulation process aiming to model (1) the internal irradiation set-up, characterizing particles entering the nucleus belonging to a planar colony, and (2) the DNA damage induced in that specific nuclear shape, was adopted. The uptake assay, immunofluorescent staining and

imaging of the cellular morphologies were previously established (13,18) and details are described in the Supplemental materials.

### **Modelling the internal irradiation set-up**

Cellular polygonal mesh models from representative 4Pi confocal microscopic images of human osteosarcoma cells (U2OS-SSTR<sub>2</sub>) were used to model 3 cellular morphologies in GDML format. Each cellular shape consists of cellular membrane (CM), cytoplasm (Cy), Golgi apparatus (G) and nucleus (N). The latter was simplified by either an ellipsoid or an elliptic cylinder, preserving its original volume and proximity to the other cellular compartments (Figure 1A). The geometrical characteristics of the 3 cells are summarized in Table 1.

Simulations were performed on Geant4.10.06 (19–21). A parameterization process replicating each cellular shape, and its sub-compartments, within an array was used to create 3 planar populations of 50 adjacent cells of same shape (Figure 1B). The number of cells was chosen to allow a cell layer dimension greater than the average range of <sup>177</sup>Lu β-particles ( $R_{CSDA\_Eavg} = 270 \mu m$ ,  $R_{CSDA\_Emax} = 1.76 mm$ ). Indeed, the <sup>177</sup>Lu - cross dose (i.e. the absorbed dose delivered by surrounding cells to a target cell) decreases exponentially with distance and hence increasing the planar cellular cluster size with additional cell layers after a given value (on average 3-4 cell layers) would not significantly contribute to the total absorbed dose received by the nucleus of the central cell (13). The computational memory consumption was drastically reduced by the Geant4 parameterization process, since the tessellated geometries (i.e. polygonal mesh) used to model each cellular morphology were stored only once in the memory. The cells were attached to the bottom of a water cylinder, as described later in the text.

The decay spectrum of  $^{177}\text{Lu}$  is reported in Supplemental Table 1 for reference. In this study the full continuous  $\beta$  (RADAR) and discrete internal conversion (IC) electron (ICRP107) spectra were simulated, whilst photon and Auger electron emissions were neglected. Photon emissions are considered negligible for cellular dosimetric purposes (22) and Auger electrons are unlikely to reach the nucleus from cytoplasm or Golgi. Each of these source components were sampled separately in order to distinguish the contribution of  $\beta$  and IC-electrons coming from the same nuclear transition.

The radioactive source ( $^{177}\text{Lu}$ -DOTATATE) was assumed to be instantly and permanently incorporated within the cell (internalized), while a smaller portion remained membrane bound based on the uptake measurements. The probability of emission within the cell (73%) or the membrane (27%) was sampled according to previous uptake experiments with 2.5 MBq/ml (13) and hence, following the average cell population behavior. Two internalization hypotheses (i.e. Golgi or cytoplasm) were investigated (Figure 2) and due to the impossibility of distinguishing an intra-organelle variation in the activity distribution, the activity was sampled uniformly in each cell compartment (Golgi, cytoplasm and CM). The radioactive source was sampled in all the cells simultaneously.

The unspecific contribution of the medium to DSB induction was investigated in a separate simulation for one nuclear geometry (cell 1), given that the absorbed dose from medium to nucleus is not significantly influenced by the nuclear volume. Here, the source was uniformly distributed in a cylinder with size corresponding to the maximum range of  $^{177}\text{Lu}$ -beta particles (diameter, height = 1.76 mm).

The “Livermore” low energy physics models were adopted in Geant4 to track electrons down to an energy of 100 eV while the default production threshold of secondary electrons was set to 0.2

$\mu\text{m}$  (adapted to cell nuclear volumes) which corresponds to 1.75 keV in liquid water. Atomic de-excitation processes, such as Auger cascades and fluorescence, were included in the simulations. The chemical composition of CM, cytoplasm, Golgi and nucleus was the same as water ( $\rho = 1 \text{ g/cm}^3$ ) (NIST database). The position, direction, energy, compartment of emission and event identifier (i.e. “event ID”), which identifies particles derived from the same primary, were recorded for each particle entering the nucleus of the central cell, assumed as representative for the cell population. The number of particles run per simulation ensured a phase space (PHSP) file larger than 1 million particles.

### **DNA damage simulation**

DSB yield calculations were carried out with a computational chain (23) using the Geant4-DNA (24–27) extension of the Geant4 toolkit (version 10.1). In this case, all the electron interactions are simulated in a discrete manner (i.e. step-by step) down to the electron thermalization, making possible the track structure simulation required at the nanometer scale; as such, they simulate explicitly all interactions and do not use any production cut. The simulation chain include not only these physical interactions but also the physico-chemical, and chemical stages within representative cell nucleus with DNA structure (Supplemental Figure 1). Therefore, simulations were performed to compute DNA strand breaks (i.e. direct damage of the DNA backbone and indirect damage of the DNA backbone-sugar leading to strand breaks). DSBs were scored from the simulated strand breaks as defined in (13), i.e., at least two strand breaks located in opposite strands and separated by less than 10 base pairs. Genomic content of cell nuclei composed of chromatin fibers in the G0/G1 phase of the cell cycle was generated with the DNAFabric software (28,29). The simulation chain coupled to these geometries allowed the calculation of DSBs per source particle (SP) reaching the nucleus, as recorded in the PHSP file. Source particles characterized by the same event

ID, whose tracks are related to the same primary, were simulated together until a relative standard deviation on the average DSBs per source particle of 5% was reached. The DSB yields are reported in terms of DSBs per source particle and per Gbp ( $N_{DSBs/(SP\ Gbp)}$ ) and, for the calculations of total number of DSBs, all nuclei are assumed to have 6 Gbp ( $N_{DSBs/SP}$ ).

### DSBs calculations and measurement

The output of the DSB simulations ( $N_{DSBs/SP}$ ) is converted to the number of DSBs corresponding to an added activity of 2.5MBq/ml, as follows:

$$N_{DSBs} = \left( (n_M p_{M \rightarrow N} + n_C p_{C \rightarrow N}) \times N_{DSBs/SP} \right)_{\beta} + 0.15 \left( (n_M p_{M \rightarrow N} + n_C p_{C \rightarrow N}) \times N_{DSBs/SP} \right)_{IC-electrons}$$

Where  $n_M$  and  $n_C$  are the number of decays cumulated in a time interval  $T_h$  within the medium and the cells (membrane bound and internalized), respectively;  $p_{M \rightarrow N}$  and  $p_{C \rightarrow N}$  are the probabilities from medium or cells to reach the nucleus of the central cell. The factors related to the cell contribution ( $n_C p_{C \rightarrow N}$ ) comprise either Golgi or cytoplasm irradiation. The total  $N_{DSBs}$  is then calculated accounting for the contribution of  $\beta$  and IC-electrons, weighting on the corresponding probabilities of emission from  $^{177}\text{Lu}$  (i.e. 1 and 0.15 per decay, respectively).

The simulated results are compared to the experimental number of DSBs/cell measured by 53BP1 foci formation as previously reported (18). Briefly, Z-stack imaging was performed using a TCS SP5 confocal microscope (Leica) and foci were counted from at least 50 cells of 2 independent experiments using Image J software (30) (settings: median blur 1.0, maximum projection and find maxima, noise tolerance 75 for cells and 100 for slices). The not treated average DSBs level was subtracted from the measured data.

## **Detailed dosimetric characterization of the nucleus irradiation**

Source particles entering the nucleus of the central cell for each PHSP file were compared in terms of energy and position/direction of entrance in the nucleus.

Furthermore, separate simulations scoring the specific energy within the nucleus were performed for each PHSP file in order to justify the possible difference in DSB yields. Indeed, the determination of the energy distribution (and hence the macroscopic LET) of electrons entering the nucleus alone is not sufficient to characterize the relationship of the electron tracks to biological effectiveness. For this purpose, Geant4-DNA models and processes (physics list option 2) were used to enable track-structure (i.e. step-by-step) simulations of electrons in liquid water down to the meV energy range. The energy deposited event by event within the nucleus was used to score the specific energy distribution.

## **Statistical analysis**

The unpaired t-test (2 group samples) and one-way Anova (more than 3 group samples) were used to assess the significant difference ( $p < 0.05$ ) between sets of data (DSB yields, probabilities to reach the nucleus , number of SP traversing the nucleus ) within the shape modeling and source localization comparison. A two-way Anova was performed, as well, to understand how cellular shapes and source localizations, in combination, affect these sets of data.

## **RESULTS**

### **Cellular shape and internalization compartment influence the level of nucleus irradiation**

The probability of reaching the nucleus from the cell ( $p_{C \rightarrow N}$ ) is 3 to 4 times higher than from the medium ( $p_{M \rightarrow N}$ ) due to geometric factors. Moreover,  $p_{C \rightarrow N}$  significantly depends on the proximity

and distribution of the cell compartment with respect to the nucleus, as shown in Figure 3. The more the radioactive cell compartment closely surrounds the nucleus, the more  $p_{C \rightarrow N}$  increases, as for the Golgi in cell 3.

In order to include the contribution of the medium in the previous comparison, Figure 3B reports the number of  $^{177}\text{Lu}$  disintegrations reaching the nucleus per particle type and cell corresponding to 2.5 MBq/ml of added activity. Once again, cell morphology and source location have a strong combined effect to the number of tracks reaching, and hence potentially damaging, the nucleus and its genetic content.

### **DSB induction is significantly different when $^{177}\text{Lu}$ is located inside the cell or in the medium**

The DSB yields normalized to the amount of genetic material (Gbp) and source particle reaching the nucleus ( $N_{DSBs/(SP\ Gbp)}$ ) differed significantly depending on the irradiation geometry (i.e. source and target shape and size in relation to particle track). The DSBs induced by the beta particles in the medium are significantly lower than the ones induced by the 3 cell sources. Furthermore, even though the difference among the 3 cell morphologies is not significant, the localization (i.e. Golgi or cytoplasm) and the specific shape of the radioactive cell compartment cause a spread in the biological damage, as shown in Figure 4A.

The variation in DSB yields among the analyzed cells is caused by the position and direction of particles entering the nucleus, which significantly depend on the cellular morphology. These characteristics affect the hit probability, which is the probability of having an energy deposition event potentially causing a damage to the DNA structure. Specifically, the broader angular distribution of the scattered beta particles entering the nucleus from the medium, increases the electrons which traverse it with a lower efficiency (greater polar angle). The same applies to the

comparison between cell morphologies and cell compartments (Figure 4B-4C); in this case, the difference is predominantly less noticeable given the overall similar source-to-nucleus proximity. Indeed, the proportion of events causing a damage for the internalized source ranges between 0.91 - 0.93 for nucleus 1, 0.45 - 0.62 for nucleus 2 and 0.46 - 0.67 for nucleus 3, depending on internalization hypothesis and emission type. If the source is in the medium, the same range is reduced to 0.39 - 0.49. To understand these differences, we analyzed the distribution of energy deposition events in the nucleus by means of microdosimetric simulations.

Dividing the DSB yields by the mean absorbed dose delivered per particle source in each nucleus, the number of DSBs/(Gy Gbp SP) ranges between 2.3 and 3.0, depending on internalization hypothesis and particle type.

In terms of DSB complexity, i.e. the number of close strand breaks that can be attributed to the same DSB, there is no significant difference among cell morphologies and type of particle emitted ( $\beta$  versus IC-electrons). The proportion of simple DSBs (i.e. DSBs made of 2 single strand breaks - SSBs) ranges between 79.7% and 92.2% with respect to the complex DSBs (i.e. DSBs made of 3 or more SSBs with at least one of them located in an opposite strand to the others), as expected for low-LET radiation.

### **The specific energy in the nucleus explains the DSB yields difference between cell and medium source**

The source localization does not significantly affect the energy distributions of particles entering the nucleus (Figure 5A-B), explaining why the DSB range/Gy Gbp is similar for all the cell morphologies. Indeed, the energy distributions of electrons coming from medium or cells, and hence their slowing down, is similar as well for the beta as the IC-electrons. However, the nucleus

geometry affects the electron path length, causing significant differences in the energy deposition patterns within the nucleus itself (Figure 6).

Specifically, the microdosimetric energy spectrum of particles coming from the medium is significantly shifted to lower energies with respect to all the cell sources (Figure 6, Table 2), reflecting the DSB yields comparison. The difference among cell morphologies is also the result of these spectral differences as it is evident when comparing the corresponding specific energy in Table 2 with the DSB yields in Figure 4.

### **Simulated DSBs match experimental data**

The total number of simulated DSBs per cell for 2.5 MBq/ml of  $^{177}\text{Lu}$ -DOTATATE ranges between 7 and 24 (Figure 7A-B) compared to 2 - 30 experimentally determined (Figure 7C) (18). The mean DSBs/cell correspond to 14 and 13, for simulations and experiments, respectively.

As expected, the induction of DSBs is mostly caused by beta particles, whilst the IC-electron component results to be significant only for specific cellular morphologies (Figure 7A). The medium contribution is not assumed to vary depending on the nuclear geometry, hence its relative impact strictly depends on the cell source contribution in each morphology (Figure 7B).

Linear correlations ( $R^2 = 1$ ) with slopes of 0.014 and 0.017 DSBs/cell  $\text{mGy}^{-1}$  are found between the average specific energy and the simulated number of DSBs, when assuming the internalized source in Golgi or cytoplasm, respectively (Figure 7D). Absorbed dose values corresponding to 2.5 MBq/ml are reported in Supplemental Table 2 and the absence of correlation when using average absorbed dose calculations is highlighted in Supplemental Figure 2.

## DISCUSSION

Modeling DNA damage following TRT exposure can lead, through comparison with experimental data, to a better understanding of the underlying mechanisms of this treatment modality. Ultimately, it will allow evaluation of treatment efficacy granting the flexibility of a simulation environment, and as such, new opportunities for the evaluation of novel radiopharmaceuticals. The first step towards this aim was made here, in which we accounted for detailed cellular morphologies and activity distributions to replicate a typical ( $^{177}\text{Lu}$ -DOTATATE) planar *in vitro* TRT environment and tested the feasibility of performing DSBs simulations through a simulation chain created for external radiation exposure.

The importance of an improved cellular morphology modelling has already been highlighted for macrodosimetric calculations (i.e. S-values) involving a planar colony of cells exposed to  $^{177}\text{Lu}$ -DOTATATE (13), however its impact on DSBs yields had never been assessed before. Noticeably, detailed cellular morphology modelling and activity localization sampling resulted indispensable to correctly estimate the amount of induced DSBs, since they significantly influence (1) the probability of electrons reaching the nucleus and (2) the distribution of track lengths within the nucleus itself. The volumetric and shape characterization of the nucleus is fundamental to correctly evaluate the energy deposition pattern, as well.

Interestingly, the energy distributions of electrons entering the nucleus from the medium is not shifted to lower energies with respect to the cell source. For this reason, the difference in DSBs yields induced by unbound (i.e. medium) and bound (i.e. cell) activity is not caused by different energy spectra of particles entering the nucleus. Indeed, in our simulations, the portion of electrons with energy below 10 keV, i.e. the electrons with the highest RBE for DSB induction, resulted to be very similar (within 1%) in all PHSP files, indicating a possible similarity in the relative

biological effectiveness (RBE) for DSBs induction (31). Instead, the energy deposition pattern within the nucleus reflected the difference in DSBs yields, underlying the importance of both microdosimetric analysis and activity characterization at cellular scale to predict biological effects for low-LET radiation, as well. Microdosimetry, in fact, accounts for the characteristics of the electrons tracks (i.e. finite range and change of LET along the track, energy-loss straggling,  $\delta$ -rays escape and angular scattering) in order to correctly evaluate the concentration of the energy transferred to the nucleus and hence the biological effectiveness of the source particles.

Altogether, the need for detailed cellular morphology modelling, accurate sampling and a microdosimetric framework able to explain biological effects, as highlighted in this work, is in striking contrast with the current dosimetric approach of implementing simplifying cell models (i.e. concentric spheres) and a semi-analytical radiation transport model adopting the continuous-slowing-down approximation (32). Indeed, not accounting for the typical complexity and heterogeneity at the cellular or multi-cellular level and relying on averaged large-scale dosimetry might be the reason for missing dose-response correlations that could be translated on a clinical scale.

To our knowledge, this is the first study simulating DSBs formation following  $^{177}\text{Lu}$ -DOTATATE exposure while including all stages of damage induction, hence we compared our results with photons (producing similar secondary electron spectra) and electron beam irradiation data available in literature. The number of DSB yields of this work ( $2.3 - 3.0 \text{ DSBs/Gbp}^{-1} \text{ Gy}^{-1} \text{ SP}^{-1}$ ) resulted to be comparable with the study of Tang et al (33), in which the simulated results ranged between 3.5 and 2.8 DSBs/(Gbp Gy) for 220 kVp X-rays and 4MV X-rays irradiations, respectively. Similarly, Nikjoo et al. (34) estimated a DSB yield for 100 keV electrons of 3.32 DSBs/(Gy Gbp), assuming 6 Gbp of genetic material and  $3.9 \cdot 10^{-12} \text{ Da/cell}$ . In both cases, the portion of complex DSBs was

similar to this study. In this work, the DSB complexity was independent from the source localization. Hence, repair mechanisms acting on DSBs caused by medium or cell source will be most likely the same.

It should be noted that the parameters implemented in the simulations to score DNA damage induction can strongly influence the final DSB yields. The good agreement reached with the aforementioned studies could be explained by the similar parameters set to score direct and/or indirect strand breaks. Indeed, increasing the chemical simulation end-time from 2.5 ns (as set in this work) to 10 ns would increase the number of DSBs by a factor of  $\sim 1.3$  (33) and either decreasing the threshold for direct SSB induction from 17.5 eV to lower values or introducing a linear probability between 5 eV and 37.5 eV would significantly affect the total number of DSBs (34,35). We did not study how these parameters variation would affect our calculations, given that our results were already comparable with the experimental data (18) and the computational time required for these simulations is considerably long.

Nevertheless, our simulated results represent a lower bound on the average number of DSBs and their complexity. Our modelling approach, in fact, neglects the contribution of photons and Auger electrons emitted by  $^{177}\text{Lu}$ , the resonant formation of strand breaks by very low energetic electrons ( $< 20$  eV) (36–38), the induction of non-DSB oxidative clustered DNA lesions and the consequence of sugar and base residues repair which can increase the final strand breaks yield. In addition, cells exposed to  $^{177}\text{Lu}$ -DOTATATE are not synchronized in a specific cell-phase, as we assumed for the purpose of simplification, but are characterized by a distribution of radio-sensitivity, associated to their cell-phase, that should be accounted for when simulating different nuclei. Lastly, we did not include the possibility of DSB repair, given that repair mechanisms involved in TRT have not been fully understood yet. Specifically, during TRT since DNA damage induction persists over time,

induction and repair occur simultaneously and hence repair mechanisms might differ significantly from EBRT. However, our approach might be justified by the very low DSB reduction pace (0.96 % in 4h), or better, the substantial equilibrium between induction and DSBs repair, indicated by the average (among the cell population) experimental decrease in the number of 53BP1 foci over 3 days (18). It should be noted, however, that sub-lethal damage repair differs among the cell population depending on cell-phase and dose rate variation too.

Moreover, the DSBs are measured by means of 53BP1 foci, i.e. repair foci, and hence might be slightly underestimated, as well. Indeed, only breaks in which repair is induced are accounted for with this measurement and the fluorescently labeled compound might not successfully bind to the 53BP1.

At present, only Uta Eberlain et al. proved the existence of a correlation (with slope 0.0127 DSBs  $\text{mGy}^{-1} \text{ cell}^{-1}$ ) between the absorbed dose to blood of patients undergoing  $^{177}\text{Lu}$ -DOTATATE treatment and the induction of DSBs, measured by the co-localized biomarkers  $\gamma\text{H2AX}$  and 53BP1 (39). Remarkably, we found a similar number of DSBs per cell and per mGy (0.014 vs 0.017 DSBs  $\text{mGy}^{-1} \text{ cell}^{-1}$ ), which serve as further validation of our computational approach.

Further improvements in the computational chain pertain to the inclusion of base damage affecting the DSBs complexity (40), different oxygen levels in the nuclear medium, different cellular shapes in a single exposure scenario, intra-organelle variation of the internalized activity fraction, realistic cellular media and a more representative distribution of the genetic material, according to the cell cycle and including realistic proportions of euchromatin and heterochromatin. Some of these improvements are currently being developed by the Geant4-DNA community and will be included in future simulations. More studies investigating the temporal variation of dose rates over time

against biological phenomena such as DNA repair capacity and cell cycle progression over the cell population would help to further improve biophysical modeling, as well.

To conclude, in order to develop a comprehensive model, not limited to a planar *in vitro* application but representative of an *in vivo* tumor scenario, a 3D aggregation of cells characterized by a variable SSTR<sub>2</sub> expression should be modelled. For this purpose, the variability of SSTR<sub>2</sub> expression among cellular population samples should be analyzed by means of FACS analysis or flow cytometry, so that the intensity of the receptor staining could be normalized and used to sample a heterogeneous receptor expression among the cell population. As such various probability distributions of the SSTR<sub>2</sub> expression can be generated to test the influence on the absorbed dose estimation. Moreover, the effect of <sup>177</sup>Lu-DOTATATE on peritumoral vessels will influence tumor hemodynamics and in a lesser extent its cross-dose irradiation, which could be explicitly simulated by changing the proportion of activity bound to the vessels, according to tumor differentiation and aggressiveness. Somatostatin is known to cause vasoconstriction resulting in regional hypoxia or necrosis (41). The oxygen effect should be taken into account by modifying the chemistry processes (e.g. by adding the specific chemical processes that lead to the creation and the chemical reactions of radicals involving oxygen) or by simply correcting with the oxygen enhancement ratio for DSBs induction. Finally, even though direct radiation effects will form the major contribution to cellular responses, bystander effects and abscopal effects should be studied in tissues with low-receptor expression. Indeed, bystander signaling may be present in receptor negative cells within a matrix of receptor-positive cells but will be obscured by many other factors influencing cell survival. In order to model such effects, first studies focused on selecting relevant radiation perturbed molecular pathways or intracellular targets, whose hit by radiation initiates the emission of bystander signals (i.e. mitochondria, nuclear membrane, ribosomes, etc), should be performed

in order to inform a more systemic description of the biological response to radiation following TRT exposure.

## **CONCLUSION**

In this work we developed a simulation framework to evaluate the number of DNA DSBs occurring during *in vitro* TRT, which, through further modifications and comparison with experimental data, can lead to a better understanding of the underlying biological mechanisms of this therapy. Adopting this methodology, a good agreement with experimental data was found and a clear correlation between the absorbed dose and the average number of DSBs per cell after  $^{177}\text{Lu}$ -DOTATATE exposure has been established.

Furthermore, this work highlights the importance of overcoming classic macrodosimetric approaches to be able to investigate and find correlations with the biological response following TRT exposure, which is instrumental for personalized dosimetry.

## **DISCLOSURE**

No conflicts of interest exist.

## **KEY POINTS**

**QUESTION:** Can a simulation framework to evaluate the number of DNA double strand breaks (DSBs) induced by in vitro targeted radionuclide therapy (TRT) be established?

**PERTINENT FINDINGS:** We found a linear correlation between the mean specific energy to the nucleus and the number of DSBs/cell: 0.014 DSBs/cell mGy<sup>-1</sup> for internalization in the Golgi apparatus and 0.017 DSBs/cell mGy<sup>-1</sup> for internalization in the cytoplasm. Furthermore, we found a spread in the induction of DSBs caused by the specific shape of the radioactive cell compartment and a significant difference in the DSB yields induced by bound and unbound activity fractions.

**IMPLICATIONS FOR PATIENT CARE:** Ultimately this simulation tool will allow to understand the underlying biological mechanisms of TRT and interpret DNA-damage biomarkers. Knowledge of the physical, chemical and biological actions by TRT will lead the way to its optimization and a better response prediction in patients.

## REFERENCES

1. De Ruyscher D, Niedermann G, Burnet NG, Siva S, Lee AWM, Hegi-Johnson F. Radiotherapy toxicity. *Nat Rev Dis Prim.* 2019;5:13.
2. De Jong M, Breeman WAP, Bernard BF, et al. [177Lu-DOTA0,Tyr3]octreotate for somatostatin receptor-targeted radionuclide therapy. *Int J Cancer.* 2001;92:628-633.
3. Pouget JP, Lozza C, Deshayes E, Boudousq V, Navarro-Teulon I. Introduction to radiobiology of targeted radionuclide therapy. *Front Med.* 2015;2:12.
4. Graf F, Fahrner J, Maus S, et al. DNA double strand breaks as predictor of efficacy of the alpha-particle emitter Ac-225 and the electron emitter Lu-177 for somatostatin receptor targeted radiotherapy. *PLoS One.* 2014;9:e88239.
5. McMahon SJ. The linear quadratic model: usage, interpretation and challenges. *Phys Med Biol.* 2019;64:01TR01.
6. Thierens HM, Monsieurs MA, Brans B, Van Driessche T, Christiaens I, Dierckx RA. Dosimetry from organ to cellular dimensions. *Comput Med Imaging Graph.* 2001;25:187-193.
7. Charlton DE, Humm JL. A method of calculating initial DNA Strand breakage following the decay of incorporated 125I. *Int J Radiat Biol.* 1988;53:353-365.
8. Pomplun E. A new DNA target model for track structure calculations and its first application to I-125 auger electrons. *Int J Radiat Biol.* 1991;59:625-642.
9. Terrissol M, Peudon A, Kümmerle E, Pomplun E. On the biological efficiency of I-123 and I-125 decay on the molecular level. *Int J Radiat Biol.* 2008;84:1063-1068.

10. Piroozfar B, Raisali G, Alirezapour B, Mirzaii M. The effect of  $^{111}\text{In}$  radionuclide distance and auger electron energy on direct induction of DNA double-strand breaks: a Monte Carlo study using Geant4 toolkit. *Int J Radiat Biol.* 2018;94:385-393.
11. Semenenko VA, Stewart RD. A fast Monte Carlo algorithm to simulate the spectrum of DNA damages formed by ionizing radiation. *Radiat Res.* 2004;161:451-457.
12. Hsiao YY, Hung TH, Tu SJ, Tung CJ. Fast Monte Carlo simulation of DNA damage induction by Auger-electron emission. *Int J Radiat Biol.* 2014;90:392-400.
13. Tamborino G, De Saint-Hubert M, Struelens L, et al. Cellular dosimetry of  $^{177}\text{Lu}$ -Lu-DOTA-[Tyr3]octreotate radionuclide therapy: the impact of modeling assumptions on the correlation with in vitro cytotoxicity. *EJNMMI Phys.* 2020;7:8.
14. Carrasco-Hernández J, Ramos-Méndez J, Faddegon B et al. Monte Carlo track-structure for the radionuclide Copper-64: characterization of S-values, nanodosimetry and quantification of direct damage to DNA. *Phys Med Biol.* 2020;65:155005.
15. Strosberg J, Wolin E, Chasen B, et al. Health-related quality of life in patients with progressive midgut neuroendocrine tumors treated with  $^{177}\text{Lu}$ -DOTATATE in the phase III netter-1 trial. *J Clin Oncol.* 2018;36:2578-2584.
16. Strosberg J, El-Haddad G, Wolin E, et al. Phase 3 trial of  $^{177}\text{Lu}$ -DOTATATE for midgut neuroendocrine tumors. *N Engl J Med.* 2017;376:125-135.
17. Hennrich U, Kopka K. Lutathera®: The first FDA-and EMA-approved radiopharmaceutical for peptide receptor radionuclide therapy. *Pharmaceuticals.* 2019;12:114.

18. Nonnekens J, van Kranenburg M, Beerens CEMT, et al. Potentiation of peptide receptor radionuclide therapy by the PARP inhibitor olaparib. *Theranostics*. 2016;6:1821-1832.
19. Agostinelli S, Allison J, Amako K, et al. GEANT4 - A simulation toolkit. *Nucl Instruments Methods Phys Res Sect A Accel Spectrometers, Detect Assoc Equip*. 2003;506:250-303.
20. Allison J, Amako K, Apostolakis J, et al. Recent developments in GEANT4. *Nucl Instruments Methods Phys Res Sect A Accel Spectrometers, Detect Assoc Equip*. 2016;835:186-225.
21. Allison J, Amako K, Apostolakis J, et al. Geant4 developments and applications. *IEEE Trans Nucl Sci*. 2006;53:270-278.
22. Goddu SM, Howell RW, Bouchet LG, Bolch WE, Rao DSMC. MIRD cellular S values SNM MIRD Committee. Society of Nuclear Medicine edition; 1997.
23. Meylan S, Incerti S, Karamitros M, et al. Simulation of early DNA damage after the irradiation of a fibroblast cell nucleus using Geant4-DNA. *Sci Rep*. 2017;7:11923.
24. Incerti S, Baldacchino G, Bernal M, et al. The Geant4-DNA project. *Int J Model Simulation, Sci Comput*. 2010;1:157-178.
25. Incerti S, Ivanchenko A, Karamitros M, et al. Comparison of GEANT4 very low energy cross section models with experimental data in water. *Med Phys*. 2010;37:4692-4708.
26. Bernal MA, Bordage MC, Brown JMC, et al. Track structure modeling in liquid water: A review of the Geant4-DNA very low energy extension of the Geant4 Monte Carlo simulation toolkit. *Phys Medica*. 2015;31:861-874.

27. Incerti S, Kyriakou I, Bernal MA, et al. Geant4-DNA example applications for track structure simulations in liquid water: A report from the Geant4-DNA Project. *Med Phys.* 2018;45:e722-e739.
28. Meylan S, Vimont U, Incerti S, Clairand I, Villagrasa C. Geant4-DNA simulations using complex DNA geometries generated by the DnaFabric tool. *Comput Phys Commun.* 2016;204:159-169.
29. Tang N, Bueno M, Meylan S, et al. Influence of chromatin compaction on simulated early radiation-induced DNA damage using Geant4-DNA. *Med Phys.* 2019;46:1501-1511.
30. Schindelin J, Arganda-Carreras I, Frise E, et al. Fiji: An open-source platform for biological-image analysis. *Nat Methods.* 2012;9:676-682.
31. Nikjoo H, Lindborg L. RBE of low energy electrons and photons. *Phys Med Biol.* 2010;55:R65-R109.
32. Vaziri B, Wu H, Dhawan AP, Du P, Howell RW. MIRD Pamphlet No. 25: MIRDcell V2.0 software tool for dosimetric analysis of biologic response of multicellular populations. *J Nucl Med.* 2014;55:1557-64.
33. Tang N, Bueno M, Meylan S, et al. Assessment of radio-induced damage in endothelial cells irradiated with 40 kVp, 220 kVp, and 4 MV X-rays by means of micro and nanodosimetric calculations. *Int J Mol Sci.* 2019;20:6204.
34. Nikjoo H, O'Neill P, Wilson WE, Goodhead DT. Computational approach for determining the spectrum of DNA damage induced by ionizing radiation. *Radiat Res.* 2001;156:577-583.

35. Villagrasa C, Meylan S, Gonon G, et al. Geant4-DNA simulation of DNA damage caused by direct and indirect radiation effects and comparison with biological data. EPJ Web Conf. 2017;153:04019.
36. Boudaïffa B, Cloutier P, Hunting D, Huels MA, Sanche L. Resonant formation of DNA strand breaks by low-energy (3 to 20 eV) electrons. Science. 2000;287:1658-1660.
37. Simons J. How do low-energy (0.1-2 eV) electrons cause DNA-strand breaks? Acc Chem Res. 2006;39:772-779.
38. Martin F, Burrow PD, Cai Z, Cloutier P, Hunting D, Sanche L. DNA strand breaks induced by 0-4 eV electrons: The role of shape resonances. Phys Rev Lett. 2004;93:068101.
39. Eberlein U, Peper M, Fernández M, Lassmann M, Scherthan H. Calibration of the  $\gamma$ -H2AX DNA double strand break focus assay for internal radiation exposure of blood lymphocytes. PLoS One. 2015;10:e0123174.
40. Nikjoo H, O'Neill P, Terrissol M, Goodhead DT. Quantitative modelling of DNA damage using Monte Carlo track structure method. Radiat Environ Biophys. 1999;38:31-38.
41. Reubi JC, Schaer J, Laissue JA, Waser B, Cancer E, Re- EC. Somatostatin receptors and their subtypes in human tumors and in peritumoral vessels. 1996;45:39-41.
42. Reed R, Houston TW, Todd PM. Structure and function of the sarcolemma of skeletal muscle. Nature. 1966;211:534-536.
43. Mitra K, Ubarretxena-Belandia I, Taguchi T, Warren G, Engelman DM. Modulation of the bilayer thickness of exocytic pathway membranes by membrane proteins rather than cholesterol. Proc Natl Acad Sci U S A. 2004;101:4083-4088.

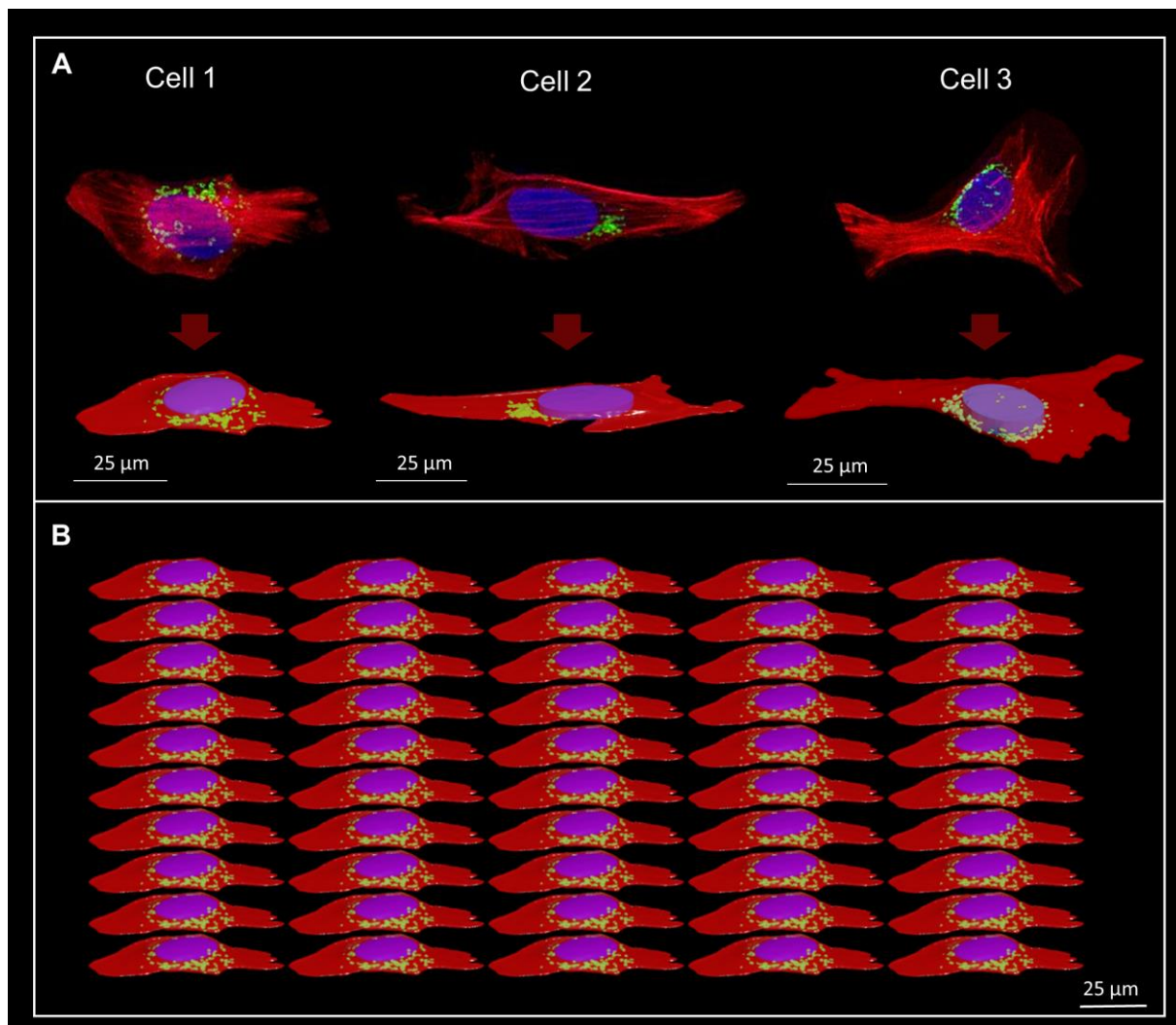


**FIGURE 1.** Cellular morphologies. A) 4Pi confocal microscope images with the corresponding polygonal mesh structures. B) Example of a cell population representing the modelled planar cellular cluster in Geant 4 (perspective view) where all cells are identical. The nucleus, Golgi and cytoplasm are represented in blue/purple, green and red, respectively. The cell population models reproduce a confluence level of  $50\% \pm 5\%$ , estimated from radiobiological observations. The geometrical characteristics of the 3 cells are reported in Table 1.

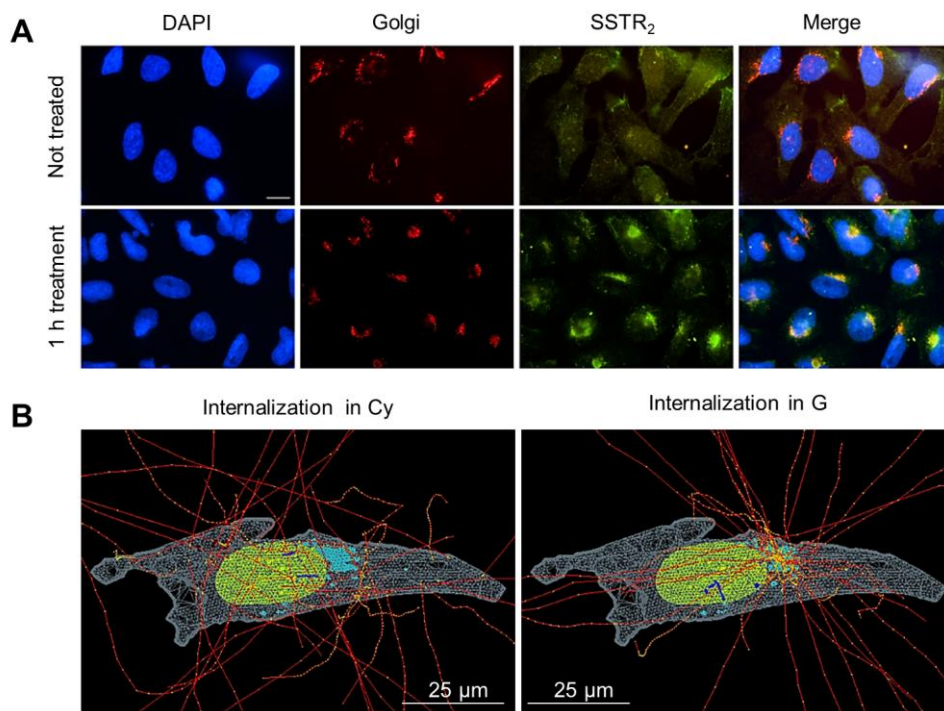


**FIGURE 2.** Immunofluorescent staining of U2OS-SSTR<sub>2</sub> cells and corresponding simulation hypotheses. A) From left to right the image reports nucleus , Golgi and SSTR<sub>2</sub> stainings for not treated cells (above) and cells incubated with DOTATATE (below). The merged image at the end highlights the co-localization of SSTR<sub>2</sub> with the Golgi apparatus after 1 h of incubation with DOTATATE. Scale bar = 5  $\mu\text{m}$ . B) Example of internalized source simulation for cell morphology 2. The nucleus, Golgi and cytoplasm are reported in green, light blue and light grey, respectively. The electron tracks are drawn in red, with yellow energy deposition points, which become blue when traversing the nucleus .

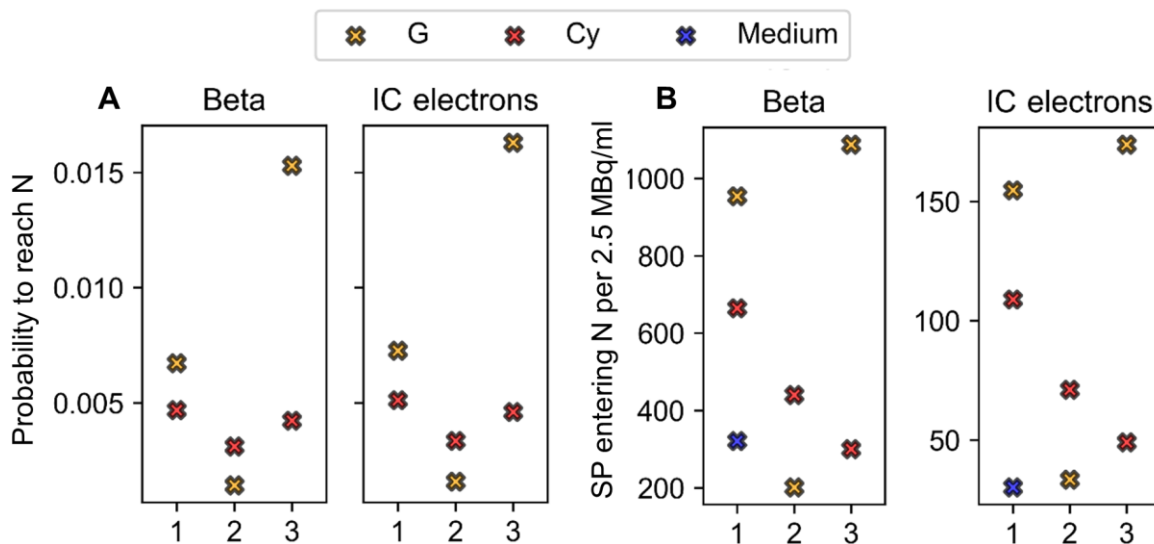


**FIGURE 3.** Comparison between A) probabilities and B) number of source particles (SP) entering the nucleus for the 3 cell models, as indicated by the x-axis, and 3 source localizations (Cy, G - including the contribution of CM - and medium when comparable to cell sources), including planar cross-irradiation. The number of particles entering the nucleus refer to 2.5 MBq/ml of added activity to which the experimental data corresponds. The medium contribution is assumed to be the same for the 3 morphologies based on simulations for cell 1. Each graph is subdivided into 2 windows corresponding to the 2 emission types (beta and IC = internal conversion electrons), as indicated by the titles.

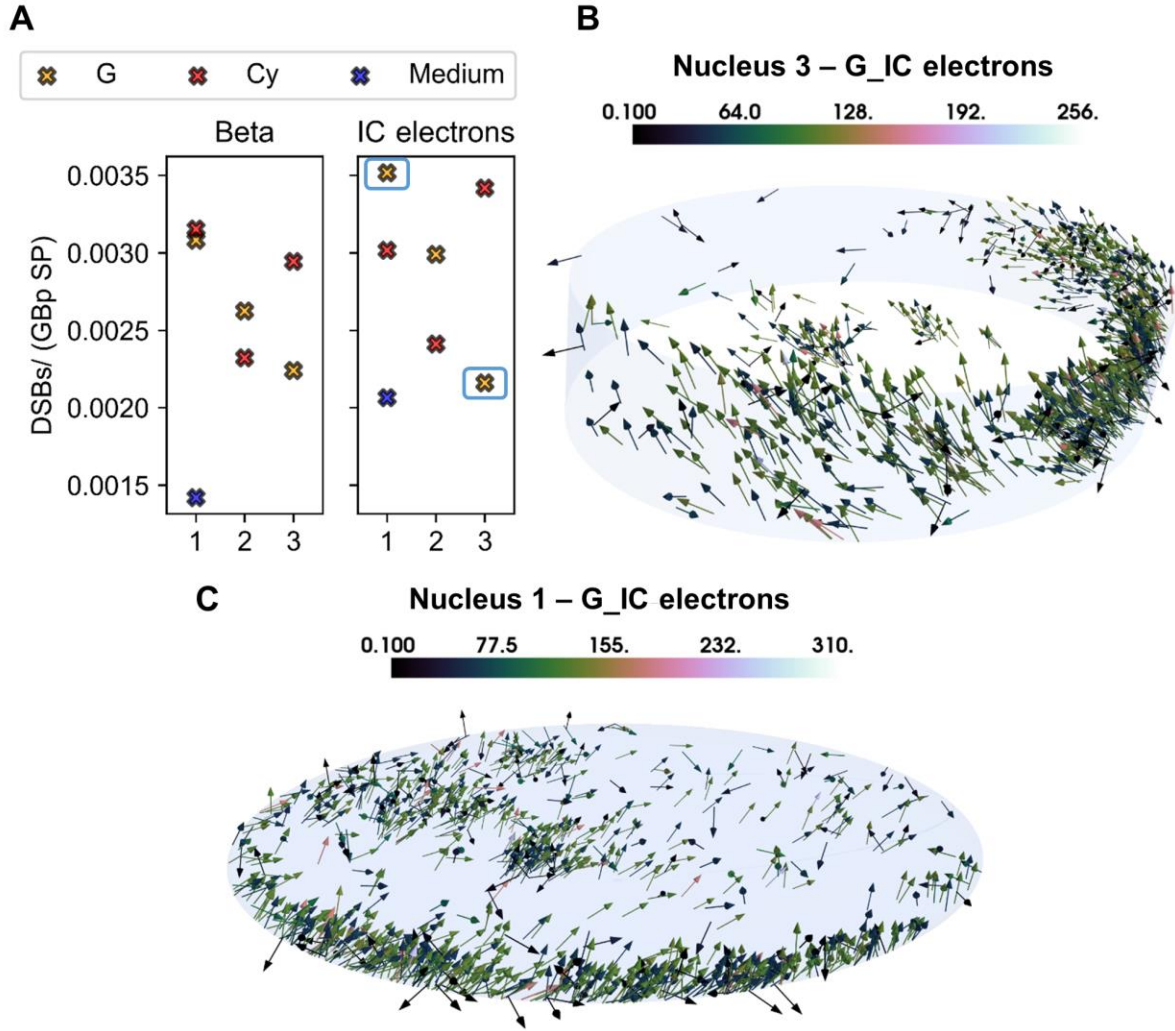


**FIGURE 4.** Simulation results and graphical explanation. A) DSB yields (DSBs / Gbp SP) comparison for 3 cell morphologies, as indicated by the x-axis, 3 source localizations (Cy, G - including the contribution of CM - and medium) and 2 emission types. The medium contribution is assumed to be the same for the 3 morphologies based on simulations for cell 1. B) Total nucleus irradiation (i.e. self- and cross-irradiation) characterizing nucleus 3 when the IC-electrons are emitted from the Golgi. C) Total nucleus irradiation (i.e. self- and cross-irradiation) characterizing nucleus 1 when the IC-electrons are emitted from the Golgi. The color bars indicate the energy at the entrance of the nucleus in keV.

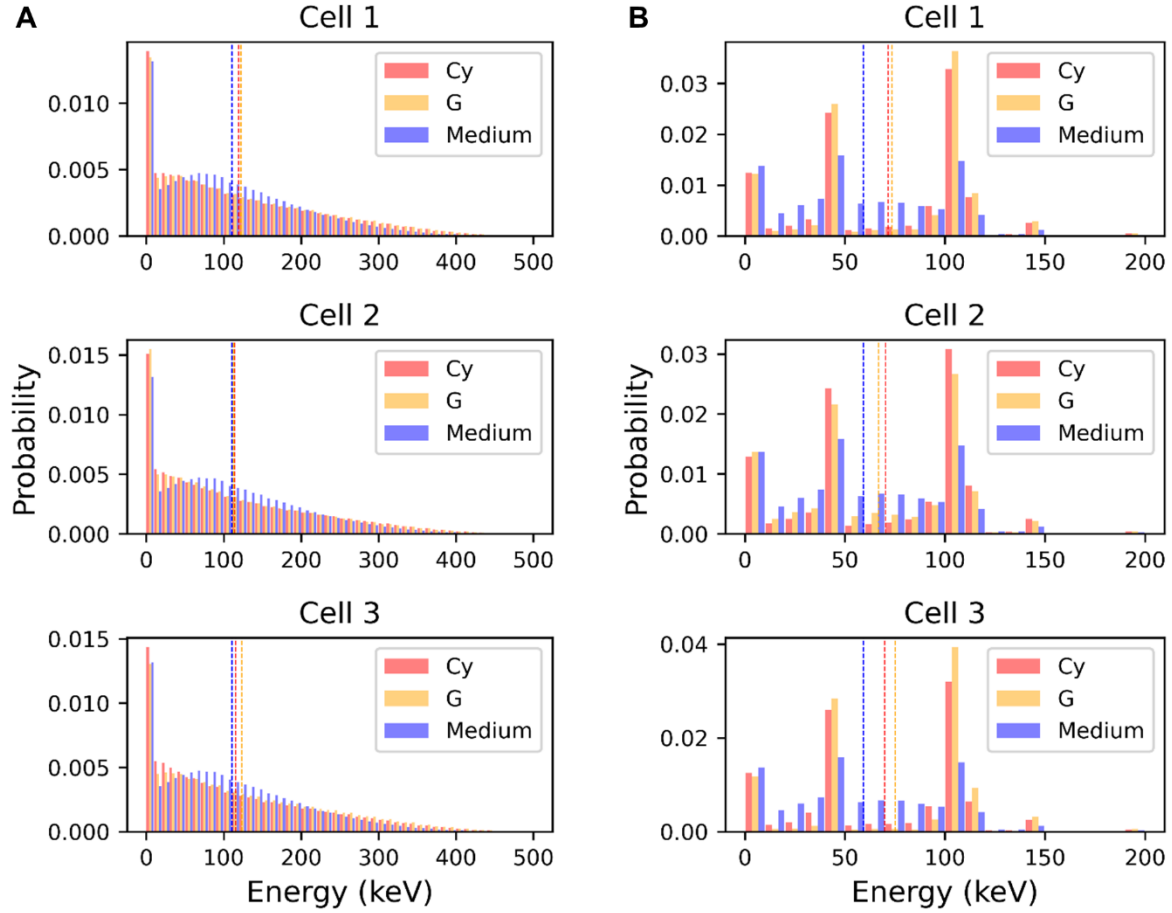


**FIGURE 5.** Energy spectra of electrons entering the nucleus of the 3 cell morphologies, as indicated by each title. A) Distributions corresponding to beta particles. B) Distributions corresponding to IC-electrons. Each color corresponds to 3 source localizations (Cy, G - including the contribution of CM - and medium), as indicated by the legend. The dotted lines indicate the mean value of the energy spectra. The spectrum of the medium is assumed to be the same as cell 1 for the 3 morphologies and replicated in each graph for comparison with cell sources. The energy bin is 10 keV.

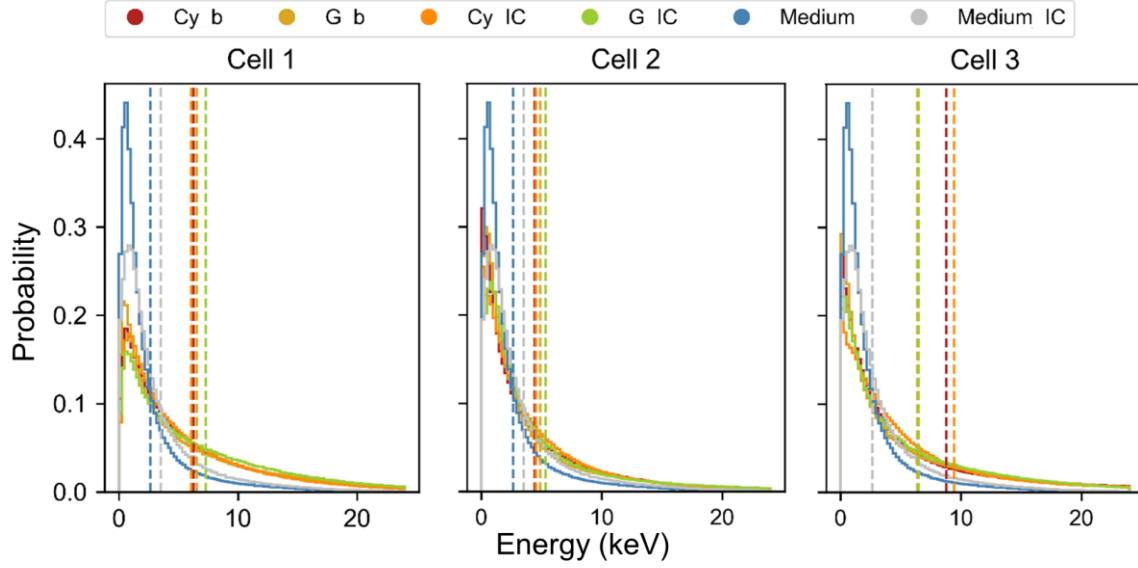


**FIGURE 6.** Probability density functions of the energy deposited per particle in the nucleus of the 3 cell morphologies, as indicated by the title of each window. Each distribution corresponds to 3 source localizations (Cy, G - including the contribution of CM - and medium) and 2 emission types (beta and IC = internal conversion electrons), as indicated by the legend. The dotted lines indicate the mean value of the microscopic energy distributions, from which the mean specific energy ( $z$ ) is evaluated (Table 2). The spectrum of the medium is assumed to be the same as cell 1 for the 3 morphologies and replicated in each graph for comparison with cell sources.

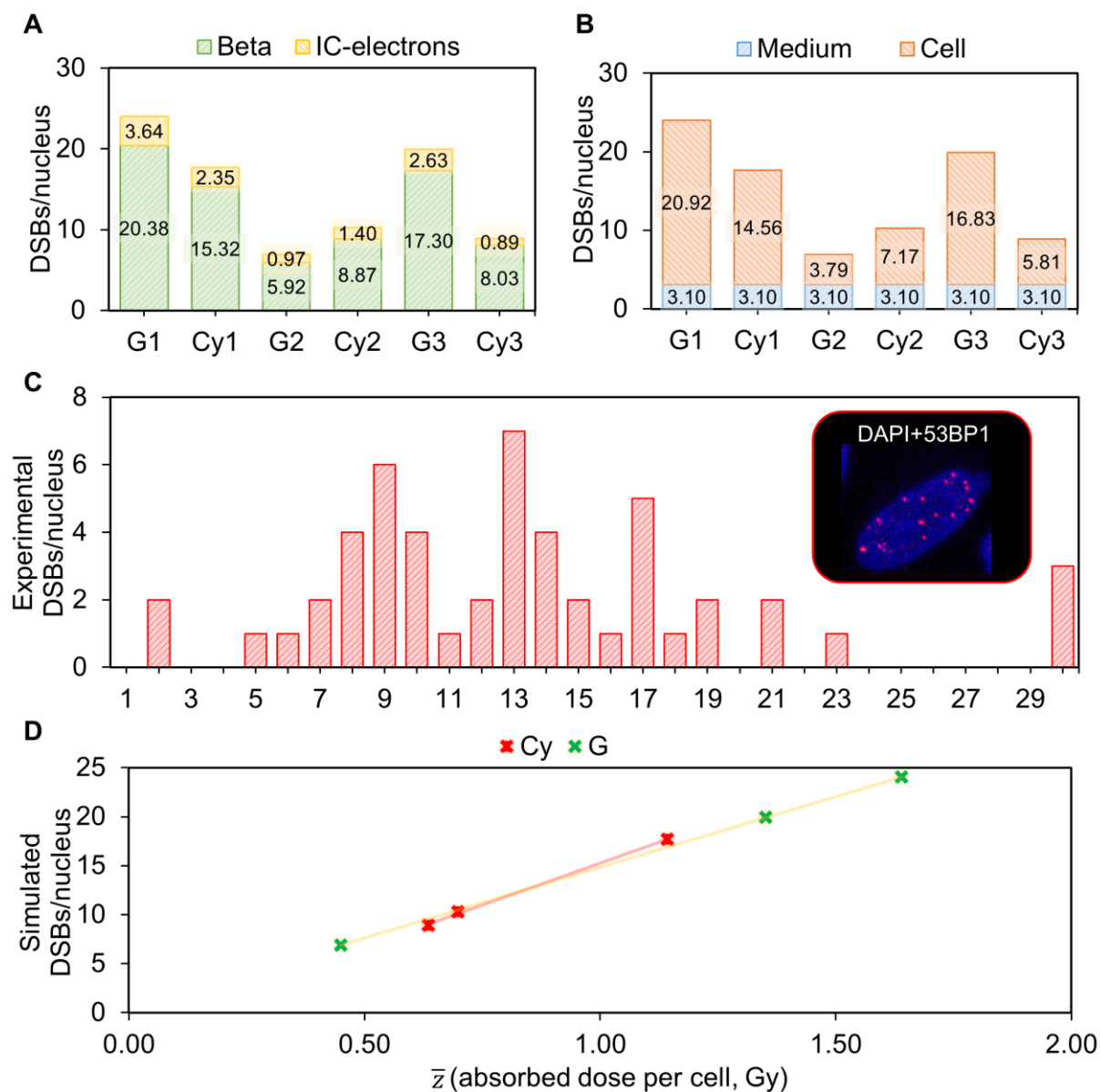
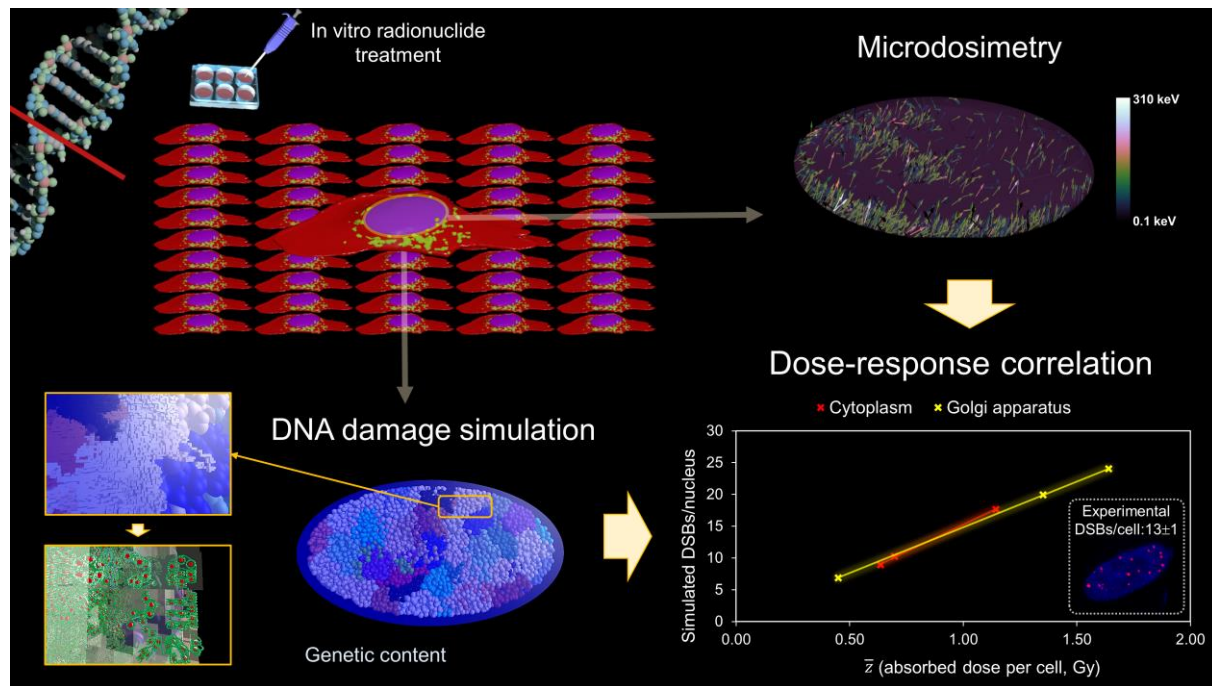


**FIGURE 7.** DSB simulations, comparison with experimental data and correlation with absorbed dose to nucleus . A) Simulated number of DSBs/nucleus corresponding to the 3 cell morphologies and internalization hypotheses (Cy VS G – including CM) indicating the contribution of each particle type (beta –IC electrons) by color bar. B) Simulated DSBs/nucleus corresponding to the 3 cell morphologies and internalization hypotheses (Cy VS G – including CM) indicating the contribution of medium or cell source (internalized and membrane bound) by color bar. C) Experimental DSBs/nucleus for 30 cell morphologies (1-30) with an inset DAPI+53BP1 image. D) Simulated DSBs/nucleus vs. absorbed dose per cell (Gy) for Cy and G hypotheses.

Frequency histogram of the experimental number of DSBs/nucleus induced by 4h of 2.5 MBq/ml  $^{177}\text{Lu}$ -DOTATATE, measured by 53BP1. D) Linear correlations between the absorbed dose to the nuclei and the simulated number of DSBs when the internalized source is located in the Cy (red) and in the G (green).

## Graphical Abstract



Volume ( $\mu\text{m}^3$ )	Cell 1	Cell 2	Cell 3
Cytoplasm	3465.64	1876.58	4228.08
Golgi	68.46	24.34	63.18
Nucleus	811.79	714.71	1105.84
Size* ( $\mu\text{m}$ )	Cell 1	Cell 2	Cell 3
Cytoplasm	$\text{BB}^\ddagger$ : x = 72.24, y = 31.78, z = 5.99	$\text{BB}^\ddagger$ : x = 99.21, y = 30.86, z = 3.52	$\text{BB}^\ddagger$ : x = 88.70, y = 64.28, z = 6.29
Nucleus	$\text{E}^\S$ : a = 12, b = 8.5 c = 1.9	$\text{EC}^\S$ : a = 13, b = 7, c = 1.25	$\text{EC}^\S$ : a = 8, b = 11, c = 2
CM thickness = 0.0075 $\mu\text{m}$ (42,43)			

\*Reported in half-dimensions for nucleus,  $^\ddagger\text{BB}$  = bounding box,  $^\S\text{E}$  = ellipsoid, EC = elliptic cylinder

**TABLE 1.** Summary of the geometrical characteristics of the 3 cell morphologies.

$\bar{z}$ (Gy)	Cell 1	Cell 2	Cell 3
Cy beta	1.24	0.99	1.27
G beta	1.29	1.10	0.92
Cy IC	1.20	1.02	1.36
G IC	1.44	1.20	0.94
Medium beta		0.52	
Medium IC		0.69	

**TABLE 2.** Mean values of the specific energy per particle entering the nucleus of the 3 cell morphologies. The medium values (beta and IC-electrons) are calculated for nucleus 1 and assumed the same for the 3 morphologies.

## **Cell lines and treatment**

Experiments were performed with human osteosarcoma cells (U2OS) stably expressing somatostatin receptor type 2 (U2OS+SST2) and maintained as previously described (1). For uptake and survival experiments, cells were treated with different activity quantities of  $^{177}\text{Lu}$ -DOTATATE (IDB Holland). Molar activity was 53 MBq/nmol, radiometal incorporation >95% and radiochemical purity >90%.

## **Immunofluorescent staining and imaging of cellular morphologies**

Cells were grown on quartz coverslips (Xantec bioanalytics GmbH, Düsseldorf, Germany) in 6-well plates until ~25% confluency and fixed with 2% paraformaldehyde (Sigma Aldrich) for 15 min at room temperature (RT), permeabilized for 20 min at RT in PBS containing 0.1% Triton X-100 (Sigma Aldrich) and incubated in blocking buffer (PBS, 0.1% Triton X-100, 2% bovine serum albumin (Sigma Aldrich)) for 30 min at RT. Next, cells were incubated for 90 min at RT with the primary antibody, rabbit anti-Giantin (PRB-114C BioLegend, San Diego, CA, USA, 1/1000) diluted in blocking buffer. Following incubation cells were washed with PBS 0.1% Triton X-100 and incubated with 100nM SiR-actin (SC001 Spirochrome) and the secondary antibody (goat anti-rabbit Alexa Fluor 488 1/1000) in blocking buffer for 90 min at RT. Cells were washed with PBS and incubated with 1 µg/ml propidium iodide (Sigma Aldrich) and 10 µg/ml RNase in PBS for 30 min at RT. Cells were washed with PBS and mounted in 87% glycerol pH8.6 (Sigma Aldrich). Z-stack imaging was performed using a 4Pi confocal microscope (Leica, Mannheim, Germany) and images were analyzed using Image J software (2).

## **Uptake assay**

Membrane bound and internalized fractions were collected as described previously (1) for 2.5 MBq/ml of added activity. Samples were collected every 15 min during the 4h treatment. Gamma

counter measurements were corrected for decay and the uncertainty on estimated activity fractions in the different cell compartments was calculated as one standard deviation of 2 independent experiments, each performed in triplicate. Furthermore, the total cell number per well was measured using a CASY cell counter (OMNI Life Science).

### **DSBs assay**

To measure DNA DSBs (*I*), cells were seeded on glass coverslips in 6-well plates 1 d before the experiment. The next day, adhered cells were incubated with 2.5 MBq/ml of  $^{177}\text{Lu}$ -DOTATATE for 4h. Subsequently, cells were washed twice with PBS and incubated for different time points (0, 1, 2, and 3 d) in culture medium without radiotracers. Cells were fixed with 1 mL of 2% paraformaldehyde (Sigma Aldrich) for 15 min at room temperature (RT), permeabilized in PBS containing 0.1% Triton X-100 (Sigma Aldrich) by incubating twice for 10 min at RT, and incubated in blocking buffer (PBS, 0.1% Triton X-100, 2% bovine serum albumin [Sigma Aldrich]) for 30 min at RT. Next, cells were incubated for 90 min at RT with the primary antibody, anti-53BP1 (NB100-304 [Novus Biologicals]; 1/1,000) diluted in blocking buffer. After incubation, cells were washed 3 times for 5 min at RT with PBS and 0.1% Triton X-100 and incubated with the secondary antibody (goat antirabbit Alexa Fluor 594 [Life Technologies]; 1/1,000) in blocking buffer for 60 min at RT. Cells were mounted with Vectashield (Vector Laboratories) containing DAPI (49,6-diamidino-2-phenylindole). Z-stack imaging was performed using a TCS SP5 confocal microscope (Leica), and foci were counted from 30 to 40 cells per condition using Image J software (National Institutes of Health). Foci were considered legitimate when their size was between 20 and 100 squared pixels; foci smaller or bigger were considered background staining.

## References

1. Nonnekens J, van Kranenburg M, Beerens CEMT, et al. Potentiation of peptide receptor radionuclide therapy by the PARP inhibitor olaparib. *Theranostics*. 2016;6:1821-1832.
2. Schindelin J, Arganda-Carreras I, Frise E, et al. Fiji: An open-source platform for biological-image analysis. *Nat Methods*. 2012;9:676-682.
3. Tamborino G, De Saint-Hubert M, Struelens L, et al. Cellular dosimetry of [177Lu]Lu-DOTA-[Tyr3]octreotate radionuclide therapy: the impact of modeling assumptions on the correlation with in vitro cytotoxicity. *EJNMMI Phys*. 2020;7:8.

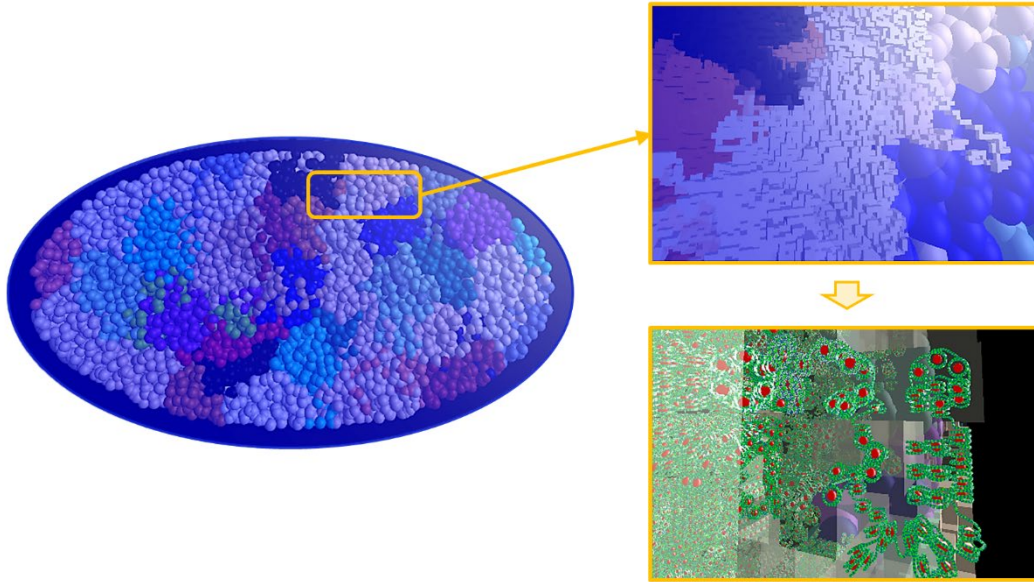
<b>Radiation</b>	<b>Boundary keV</b>	<b>N*</b>	<b>Yield N / Bq s</b>	<b>Energy MeV / (Bq s)</b>	<b>Mean energy MeV</b>
<b>X-ray</b>	E < 1	4	1.28	2.49E-05	1.94E-05
	E > 1	56	0.09	3.51E-03	3.78E-02
<b>Gamma</b>		6	0.18	3.16E-02	1.75E-01
<b>Beta</b>		4	1.00	1.33E-01	1.33E-01
<b>Auger e<sup>-</sup></b>	E < 1	6	0.82	1.13E-04	1.38E-04
	E > 1	9	0.30	1.02E-03	3.42E-03
<b>IC e<sup>-</sup></b>	E > 1	36	0.15	1.35E-02	8.74E-02

\*Number of emissions

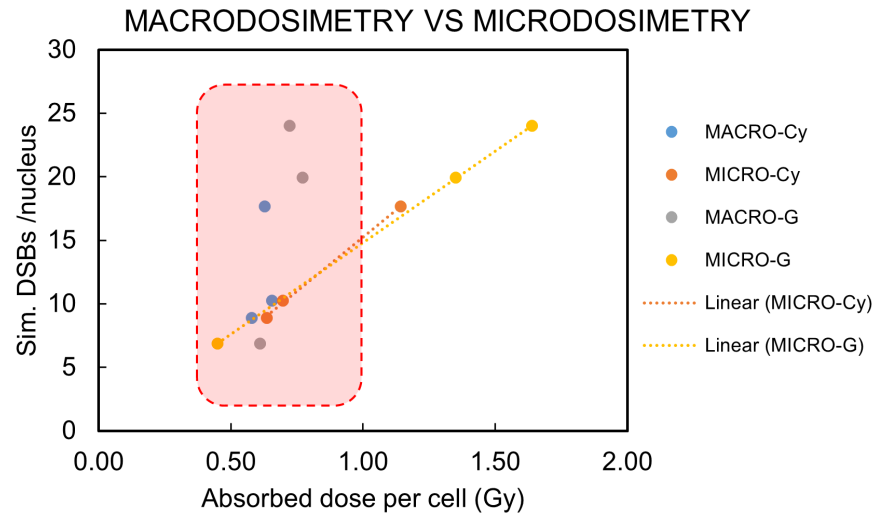
**SUPPLEMENTAL TABLE 1.** Summary of <sup>177</sup>Lu emissions, from ICRP-107. An energy boundary of 1 keV is used to discriminate penetrating and non-penetrating radiation contributions. Below the cut-off value of 100 eV, all energy is assumed to be absorbed at the site of emission.

$\bar{z}$ (Gy)	Cell 1	Cell 2	Cell 3
Cy	0.96	0.51	0.45
G	1.45	0.26	1.16
Medium		0.19	
$\bar{D}$ (Gy)	Cell 1	Cell 2	Cell 3
Cy	0.29	0.32	0.24
G	0.39	0.27	0.44
Medium		0.34	

**SUPPLEMENTAL TABLE 2.** Microdosimetric and macrodosimetric calculations corresponding to an added activity of 2.5 MBq/ml. The S-values calculations belong to a previous study (3).



**SUPPLEMENTAL FIGURE 1.** Example of nucleus filled with genetic content. In the main image, an ellipsoidal nucleus containing chromatin regions can be seen. Different colors correspond to different chromosome territories. Two zoom levels are also reported: on the left, the voxels (i.e. cubes) filling each region can be seen. On the right, the zoomed voxel shows a detail of DNA at molecular level.



**SUPPLEMENTAL FIGURE 2.** Averaged absorbed dose and mean specific energy to the nucleus versus simulated number of DSBs when the internalized source is located in the Cy or in the G.